RSC Advances

PAPER

View Article Online
View Journal | View Issue



Cite this: *RSC Adv.*, 2025, **15**, 25548

# Facile synthesis of C–$TiO_2$–$MoS_2$ nanocomposite based on commercial $TiO_2$ nanopowder for photodegradation of methylene blue†

Thi Huyen Nguyen,[ac] Tien Dung Cao,[a] Thi Phuong Mai,[a] Van Hau Tran,[a] Van Trinh Pham,[ac] Van Chuc Nguyen,[ac] Van Nhat Pham,[b] Viet Tiep Phung,[c] Ngoc Minh Phan,[c] Van Tan Tran,[d] Van Hao Nguyen,[e] Huy Tiep Nguyen[f] and Van Tu Nguyen *[a]

We present a facile synthesis method for a C–$TiO_2$–$MoS_2$-based photocatalytic nanocomposite designed for the efficient degradation of pollutant dyes, specifically methylene blue (MB) and rhodamine B (RhB). Few-layered $MoS_2$ nanosheets were exfoliated from natural bulk $MoS_2$ *via* urea-assisted ball milling. These nanosheets were then mixed with $TiO_2$ nanopowder and sodium deoxycholate (SDC) surfactant, followed by thermal annealing at 600 °C in argon (Ar) gas. The resulting $TiO_2$–$MoS_2$ mixture was found to be coated and interconnected by a carbon layer, which acted as an electron-conducting bridge and simultaneously prevented the aggregation of $TiO_2$ nanoparticles and $MoS_2$ nanosheets. The photocatalytic performance of the nanocomposite was evaluated through the degradation of MB and RhB. Remarkably, the nanocomposite exhibited excellent degradation of a high-concentration MB (RhB) solution ($10^{-4}$ M), achieving near-complete degradation within 45 minutes under UV light and 50 minutes under visible light. Furthermore, under UV irradiation, the nanocomposite reached a degradation efficiency of 99.6% with a rate constant of 0.128 $min^{-1}$, while slightly lower values were observed under visible light. A possible mechanism responsible for the enhanced MB degradation was also proposed. This strategy provides a promising pathway for the development of effective photocatalysts for practical photocatalytic applications.

Received 12th May 2025
Accepted 8th July 2025

DOI: 10.1039/d5ra03330f

rsc.li/rsc-advances



## 1. Introduction

In recent years, various water treatment technologies, including adsorption, photocatalysis, and microwave-assisted catalysis, have been widely studied for removing organic pollutants from wastewater.[1–3] Adsorption is a cost-effective and simple method with high pollutant removal efficiency, it only transfers contaminants onto solid surfaces, requiring subsequent disposal or regeneration. However, there are still several obstacles, including limited adsorption capacity, ready inactivity, secondary pollutants, and high energy consumption.[4] Microwave-assisted catalysis, a newer technique, enhances reaction rates through rapid and uniform heating at the molecular level. It offers reduced processing time and energy input, but the stability of catalysts under microwave conditions and scalability remain concerns.[4] Thus, these considerations support the need for developing efficient and sustainable photodegradation systems. Photocatalytic degradation of organic contaminants has emerged as an environmentally sustainable approach for wastewater treatment.[5,6] Titanium dioxide ($TiO_2$), available in various nanostructured morphologies, has gained significant attention as a promising photocatalyst for decomposing harmful dyes due to its high photocatalytic efficiency, excellent photostability, and non-toxic nature. Additionally, $TiO_2$ nanoparticles are readily available on the market. However, two primary limitations hinder its practical application in photocatalysis: (1) its absorption is limited to the ultraviolet region, which accounts for only about 4% of the solar spectrum, and (2) the rapid recombination of photogenerated charge carriers significantly reduces its photocatalytic efficiency.

To overcome these issues, many research groups have developed many strategies to improve further the photocatalytic

[a]*Institute of Materials Science, Vietnam Academy of Science and Technology, Hanoi, Vietnam. E-mail: tunv@ims.vast.vn*
[b]*University of Science and Technology of Hanoi, Vietnam Academy of Science and Technology, Hanoi, Vietnam*
[c]*Graduate University of Science and Technology, Vietnam Academy of Science and Technology, Hanoi, Vietnam*
[d]*University of Science, Vietnam National University, Hanoi, Vietnam*
[e]*Institute of Science and Technology, TNU-University of Sciences, Thai Nguyen, Vietnam*
[f]*University of Engineering and Technology, Vietnam National University, Hanoi, Vietnam*

† Electronic supplementary information (ESI) available. See DOI: https://doi.org/10.1039/d5ra03330f

performance of $TiO_2$, such as doping with non-metallic ions, metal ions,[7–10] depositing noble metals.[11–13] Recently, a heterostructure formation of $TiO_2$ with carbonaceous nanomaterials or narrow bandgap-semiconductors is an effective approach. Numerous previous studies have reported that combining $TiO_2$ with carbonaceous nanomaterials, for instance, carbon nanotubes,[14,15] C60,[16,17] graphene oxide,[18–20] and carbon dots[21,22] can enhance the light absorption of $TiO_2$ across the entire visible spectrum, compared to bare $TiO_2$. The enhanced light absorption was ascribed to the formation of chemical bonds (Ti–O–C) between $TiO_2$ and the carbon-based materials.[23] Crucially, carbonaceous materials act as effective electron acceptors, facilitating the transfer of electrons from the photogenerated electron–hole pairs in $TiO_2$, thereby enhancing charge separation efficiency.[24,25] However, the low visible light utilization still restricts their wide applications in environmental management.

Different from carbonaceous materials, molybdenum sulfide ($MoS_2$), a member of transition metal dichalcogenides (TMDCs), is a semiconductor with a narrow indirect bandgap of about 1.3 eV in bulk, while $MoS_2$ monolayer possesses a large direct bandgap of 1.9 eV.[26,27] This allows $MoS_2$ in the nanocomposite acts as an effective photo-absorber over the solar spectrum. Moreover, the establishment of a type-II band alignment between $MoS_2$ and $TiO_2$ promotes efficient separation of photoinduced electron–hole pairs. Consequently, $TiO_2$/$MoS_2$ composites have garnered growing attention for a wide range of catalytic applications. For instance, Wang *et al.* developed a $MoS_2$/$TiO_2$ (P25) composite photocatalyst that demonstrated enhanced photocatalytic performance in degrading methylene blue (MB) and rhodamine B (RhB) under simulated sunlight.[28] By using a two-step hydrothermal process, Chandrabose *et al.* created $MoS_2$/$TiO_2$ heterostructure nanocomposites, which demonstrated high photocatalytic activity in textile dye contaminants.[29] Tang *et al.* used a straightforward and scalable one-step sol–gel process to successfully create brown-$TiO_2$@$MoS_2$ heterostructures using 2D $MoS_2$ nanosheets exfoliated from natural bulk molybdenite. Under visible light irradiation, the maximum degradation efficiency of 94.80% and the maximum degradation rate of 0.01764 $min^{-1}$ were obtained using the heterostructure catalyst. According to experimental findings, as compared to pure brown-$TiO_2$, the creation of brown-$TiO_2$ and 2D $MoS_2$ heterostructures can improve visible light absorption, extra active sites, and the separation and transfer of photogenerated charge.[30]

Recently, Nguyen *et al.* synthesized a Z-scheme C–$MoS_2$/$TiO_2$ heterostructure *via* a hydrothermal method, utilizing a carbon layer as a connecting bridge. The resulting catalyst achieved 99% degradation of methylene blue within 60 minutes under visible light irradiation.[31] Ali *et al.* reported a simple one-step solvothermal synthesis of a C–$TiO_2$–$MoS_2$ heterostructure with visible light activity, utilizing a novel $MoS_2$ cluster compound using a novel $MoS_2$ cluster compound $[(NH_4)_2\ Mo_3S_{13}\cdot 2H_2O]$ as the precursor for the synthesis of $MoS_2$. The composite demonstrates superior photocatalytic activity under visible light for the degradation of RhB and 4-ATP compared to pure $TiO_2$. However, most $MoS_2$ samples used in these studies were synthesized from costly molybdenum and sulfur compounds, which require strict reaction conditions.[32]

Inspired by the above research, this work aims to develop new photocatalyst material based on C–$TiO_2$–$MoS_2$ nanocomposite. The proposed nanocomposite was prepared using a simple method by mixing $TiO_2$ and lab-made $MoS_2$ nanosheets with SDC solution and followed by the thermal annealing process at 600 °C in Ar gas. The resulting microstructure of the nanocomposite exhibited several key advantages for photocatalytic activity, including enhanced charge carrier separation and reduced aggregation of $TiO_2$ and $MoS_2$. The nanocomposite demonstrated effective photodegradation of high-concentration solutions of the pollutant dyes under both UV and visible light irradiation.

## 2. Experiment

### 2.1 The preparation of $MoS_2$ nanosheets

The exfoliation of bulk $MoS_2$ (99.5% with a lateral size of 2–3 μm, purchased from Macklin) was carried out by using the ball milling method. First, a powder mixture consisting of bulk $MoS_2$ and urea (in a weight ratio of 1 : 30) was weighed and added to the milling jars. Next, a specific amount of $ZrO_2$ milling balls with various diameters is added to the jars. In this experiment, the weight ratio of the powder mixture to the $ZrO_2$ balls was maintained at 1 : 30. The grinding process was then conducted at a rotational speed of 400 rpm for 20 hours to facilitate exfoliation. After grinding, the resulting mixture was dissolved in deionized (DI) water and ultrasonicated for 30 min to achieve a uniform solution. The solution was then filtered several times using vacuum filtration to remove urea residuals. Finally, the cleaned $MoS_2$ nanosheets were dispersed in DI water or other suitable solvents (Fig. S1†).

### 2.2 Preparation of C–$TiO_2$–$MoS_2$ nanocomposite

$TiO_2$ nanopowder (99.9%, anatase phase with average size ~25 nm) was sourced from Nanoshel. To prepare the mixture, 10 g of $TiO_2$ was dispersed in 300 mL of ethanol. Next, 100 mg of $MoS_2$ nanosheets was then added to the $TiO_2$ suspension. In this work, a weight ratio of $MoS_2$ and $TiO_2$ (1% w/w) was adopted from previous work.[30] The mixture was treated by ultrasonication for 60 min, followed by magnetic stirring for 30 minutes. The $TiO_2$–$MoS_2$ mixture was then obtained by employing a vacuum pneumatic system to dry the solution at 80 °C. Next, the $TiO_2$–$MoS_2$ mixture was immersed in ethanol with SDC surfactant and magnetically stirred for 60 min. The sample was then transferred to the vacuum pneumatic system for drying. Finally, the sample was annealed at 600 °C in a flow of Ar gas for 30 min to facilitate the carbonization of the SDC surfactant to obtain C–$TiO_2$–$MoS_2$ composite, as shown in Fig. S2†

### 2.3 Characterization methods

The morphologies of the as-prepared samples were examined by a field-emission scanning electron microscope (FE-SEM, Hitachi S-4800) at an operating voltage of 5 kV. High-resolution

transmission electron microscopy (HRTEM) analysis of samples were acquired by a JEOL JEM2100F microscope. The thickness of as-exfoliated $MoS_2$ was measured by an atomic force microscope (AFM, XE-100 from Park Systems). The crystallinity of the as-exfoliated sample was investigated by X-ray diffraction (XRD, D8 Advance, Bruker, Germany). Raman spectroscopy with an excitation wavelength of 532 nm was used to confirm the formation of the as-prepared samples. The distribution of elements in the nanocomposite was measured by energy dispersive spectroscopy (EDS) mapping (Ultim Max 65& JSM – IT800SHL). $N_2$ adsorption–desorption isotherms were analyzed using the BET method (TriStar II 3020, USA), while the pore volume distribution was determined from the adsorption branch of the isotherms based on the Barrett–Joyner–Halenda (BJH) model.

### 2.4 Photocatalytic activity measurement of the samples

The photocatalytic performance of the as-synthesized samples was assessed through the degradation of MB and RhB in aqueous solutions under UV light ($\lambda = 365$ nm, 3 W) and visible light (Xenon lamp, $\lambda = 450$ nm, 3 W). In every experiment, 20 mg of the sample was dispersed in 50 mL of an aqueous methylene blue (MB) solution (100 mg $L^{-1}$ $\sim 10^{-4}$ M), and the suspension was magnetically stirred in the dark for 30 minutes to achieve adsorption–desorption equilibrium of MB molecules on the catalyst surface. Subsequently, the suspension was exposed to UV and visible irradiation individually. The distance between the light source and the surface of the solution was 25 cm. The photodegradation of the dyes was monitored at 5 minute intervals. After each interval, the catalyst was removed by centrifugation, and the dye concentration in the solution was determined by measuring the absorbance at 664 nm for MB and 553 nm for RhB using a UV-vis spectrophotometer (Shimadzu UV-vis (UV – 2450))

## 3. Results and discussion

### 3.1 Characterization of as-exfoliated $MoS_2$ nanosheets

Fig. 1a shows the SEM image of bulk $MoS_2$, which has a stacked structure of multiple layers. After exfoliation, the bulk $MoS_2$ was converted into nanosheets as shown in Fig. 1b. To confirm, the AFM image revealed $MoS_2$ flakes with a typical height of $\sim$3.7 nm, indicating few-layer $MoS_2$ (Fig. 1c). The Raman spectra of bulk and as-exfoliated $MoS_2$, presented in Fig. 1d, show two key peaks (named $E_{2g}$ and $A_{1g}$), linked to the in-plane vibrations of Mo and S atoms and the out-of-plane vibrations of S atoms, respectively. Notably, the distance between these peaks ($\Delta k$) may be utilized to roughly estimate the number of layers of $MoS_2$. Fig. 1d indicates that $\Delta k$ (22.8 $cm^{-1}$) of the as-exfoliated $MoS_2$ is lower compared to that of bulk $MoS_2$ (25.6 $cm^{-1}$), suggesting the presence of few-layer structures. Fig. 1e displays the XRD patterns for both bulk and exfoliated $MoS_2$. The bulk $MoS_2$ (black curve) presents a distinctive diffraction pattern with peaks at $2\theta = 14.4°$ (002), 29° (004), 32.7° (100), 33.4° (101), 35.8° (102), 39.6° (103), 44.2° (006), 49.8° (105), 58.4° (110), and

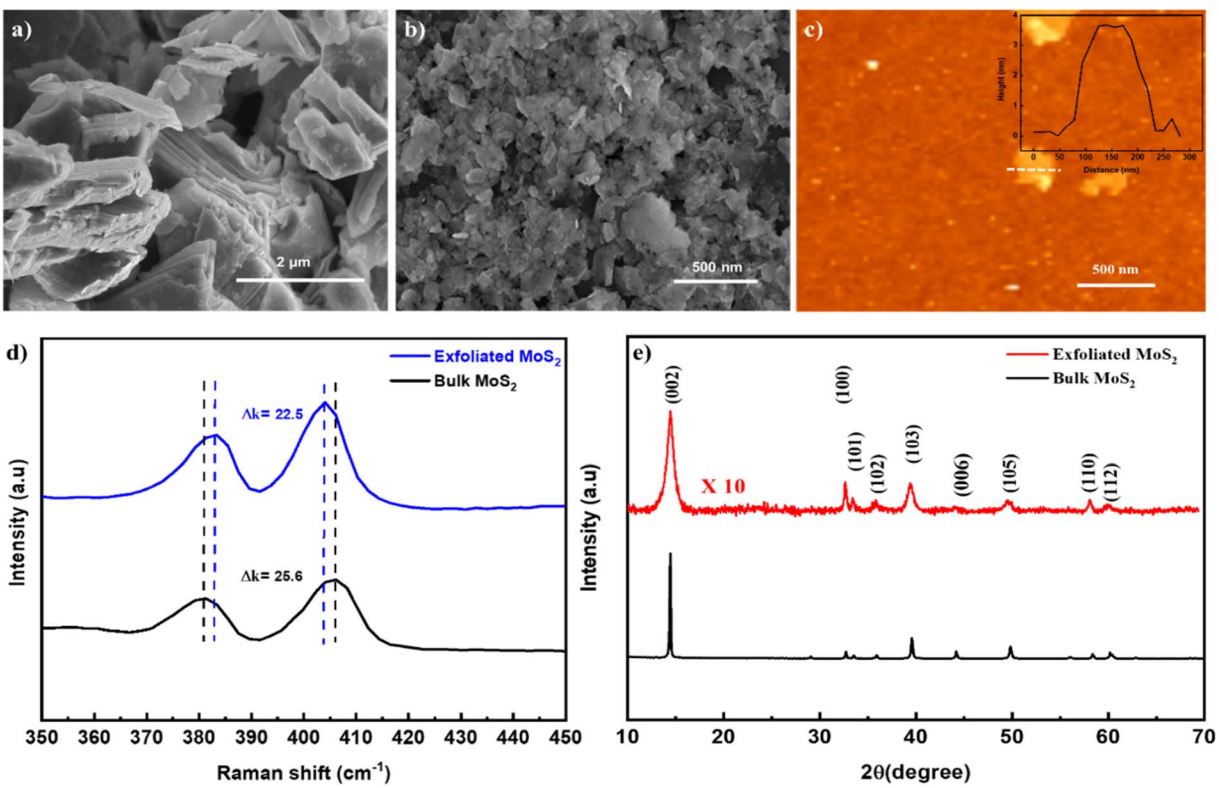


Fig. 1 (a) SEM image of bulk $MoS_2$, (b) SEM image of as-exfoliated $MoS_2$ nanosheets, (c–e) AFM image, Raman spectra, and XRD patterns of bulk $MoS_2$ and as-exfoliated $MoS_2$. Inset is the height profile of as-exfoliated $MoS_2$ in (c).

60.3° (112) (JCPDF #96-900-7661). As bulk $MoS_2$ was thinned-down to nanosheets, there was a noticeable decrease in the intensity of the peaks, along with a corresponding peak broadening, as illustrated by the red curve in Fig. 1e. The broadening and the reduction in intensity of the peak at 14.4° (002) serve as definitive indicators of the presence of thin $MoS_2$ nanosheets. Furthermore, the exfoliated $MoS_2$ nanosheets also demonstrated excellent dispersibility in various solvents, including deionized water, isopropanol, and ethanol (Fig. S1†). This enhanced dispersibility was attributed to the formation of $NH_2$ groups at the edges of the nanosheets, as confirmed by FTIR analysis (Fig. S1†).

### 3.2 Characterizations of as-prepared C–$TiO_2$–$MoS_2$ nanocomposite

The morphology of the C–$TiO_2$–$MoS_2$ nanocomposite was illustrated in Fig. 2a. However, it was difficult to distinguish $TiO_2$ nanoparticles and $MoS_2$ nanosheets due to their sizes being tiny. For clear observation, HR-TEM measurement was conducted and revealed in Fig. 2b. The HRTEM image showed that the $TiO_2$–$MoS_2$ mixture was covered and linked to each other by a carbon layer. Fig. 2b exhibits that C–$TiO_2$–$MoS_2$ nanocomposites with the lattice spacing of 0.352 nm corresponds to the (101) plane of $TiO_2$, while the lattice spacing of 0.62 nm is assigned to the (002) plane of $MoS_2$, respectively.

XRD analysis was performed to determine the crystal structure and phase composition of the synthesized samples. As shown in Fig. 2c, the XRD pattern of $TiO_2$ (red curve) exhibits distinct diffraction peaks at 25.3° (101), 37.8° (004), and 48.0° (200), which are characteristic of anatase $TiO_2$ (JCPDS #97-002-4276). The pattern of exfoliated $MoS_2$ is also included for comparison. In the case of the C–$TiO_2$–$MoS_2$ nanocomposites, the characteristic peaks corresponding to both anatase $TiO_2$ and exfoliated $MoS_2$ were clearly observed, while diffraction peaks of carbon layer could not be detected. In addition, weak diffraction peaks corresponding to rutile $TiO_2$ were detected, which can be attributed to the partial phase transformation of anatase to rutile induced by thermal annealing at 600 °C. To further confirm the formation of the C–$TiO_2$–$MoS_2$ nanocomposite, Raman measurements also were conducted. As shown in Fig. 2d, we can identify Raman active modes for the anatase phase of $TiO_2$ (black curve) at 145.1 $cm^{-1}$ ($E_g$), 400 $cm^{-1}$ ($B_{1g}$), 517.3 $cm^{-1}$ ($A_{1g}$), and 638.0 $cm^{-1}$ ($E_g$), as well as the prominent $E_{1g}$ and $A_{1g}$ peaks of thin $MoS_2$, located at 381.6 $cm^{-1}$ and 405.4 $cm^{-1}$, respectively. Additionally, the C–$TiO_2$–$MoS_2$ nanocomposite exhibited a Raman peak at 448.3 $cm^{-1}$, characteristic of the rutile phase of $TiO_2$, which is attributed to thermal annealing at 600 °C.[33] Additionally, peaks at 1346 $cm^{-1}$ and 1597 $cm^{-1}$ correspond to the D and G bands of the carbon layer (red curve) were observed.[34] These results demonstrated the coexistence of $TiO_2$, carbon, and $MoS_2$ within the C–$TiO_2$–$MoS_2$ nanocomposite.

The EDS mapping of the C–$TiO_2$–$MoS_2$ nanocomposites showed that the distribution of the carbon (C), titanium (Ti), oxygen (O), molybdenum (Mo), and sulfur (S) elements was highly uniform (Fig. 2e).

The $N_2$ adsorption–desorption isotherms and pore size distribution curves of $MoS_2$, $TiO_2$, and C–$TiO_2$–$MoS_2$ were shown in Fig. S3 (ESI†). As shown in Fig. S3,† all the samples exhibited typical type IV isotherm features and H3 hysteresis loops, confirming the presence of mesoporous structures.[35] Notably, the C–$TiO_2$–$MoS_2$ nanocomposite demonstrated the significantly higher BET surface area of 62.48 $m^2\ g^{-1}$ than that of bare $TiO_2$ (16.3 $m^2\ g^{-1}$) and $MoS_2$ nanosheets (6.7 $m^2\ g^{-1}$). The pore volumes are 0.8, 0.36, and 0.018 $cm^3\ g^{-1}$ for C–$TiO_2$–$MoS_2$ nanocomposite, $TiO_2$ nanopowder, and $MoS_2$ nanosheets, respectively. These results confirm that the C–$TiO_2$–$MoS_2$ nanocomposite has a more developed mesoporous network, which is advantageous for applications requiring high surface area and accessible porosity.

### 3.3 Evaluation of photocatalytic performance

The photocatalytic performance of the samples was evaluated by monitoring the decomposition of MB under UV irradiation, focusing on the absorption peak at 664 nm. The typical absorption peak intensity at 664 nm decreased with prolonged irradiation. Fig. 3a–e illustrates the time-dependent absorption spectra of MB degradation by bare $TiO_2$, bare $MoS_2$, C–$TiO_2$, $TiO_2$–$MoS_2$, and C–$TiO_2$–$MoS_2$ nanocomposite, respectively. As the irradiation time increased, the intensity of the absorption peak at 664 nm speedily diminished, and nearly vanished after 120 minutes for bare $MoS_2$ and bare $TiO_2$ (Fig. S4 in ESI†). Compared to only UV without catalyst (Fig. S4c†), bare $MoS_2$, $TiO_2$, and C–$TiO_2$, $TiO_2$–$MoS_2$ composite showed a faster degradation of MB after 45 min. In C–$TiO_2$–$MoS_2$ nanocomposite case, MB molecules can be degraded completely within 45 min.

The degradation percentage and degradation rate of MB are two important parameters to estimate the photocatalytic efficiency of the photocatalyst. The decline in intensity of the distinctive absorption peak at 664 nm was used to calculate the degradation percentage.

$$D(\%) = \frac{C_0 - C_t}{C_0} \times 100$$

where, $C_0$ and $C_t$ are the concentrations of MB at time 0 and $t$ (min), respectively. Where $t$ is the irradiation time. As shown in Fig. 3f, degradation percentage ($D$%) of the samples was calculated to be 33.8%, 35.8%, 43.7%, 88.9%, and 99.6% for bare $MoS_2$, bare $TiO_2$, C–$TiO_2$, $TiO_2$–$MoS_2$, and C–$TiO_2$–$MoS_2$ nanocomposite after 45 min under UV irradiation, respectively.

To determine the degradation rate of MB on the samples, a pseudo-first-order kinetic model was used in this study. The rate of degradation ($k$) of MB was derived from the slope of the linear transform ln ($C_t/C_0$), where $C_t$ and $C_0$ are the intensity values of the peak at 664 nm at time $t$ and 0, respectively. As shown in Fig. 3g, the C–$TiO_2$–$MoS_2$ nanocomposite shows the highest $k$ value (0.128 $min^{-1}$), followed by $TiO_2$–$MoS_2$ (0.05 $min^{-1}$), C–$TiO_2$ (0.013 $min^{-1}$), bare $TiO_2$ (0.011 $min^{-1}$), and $MoS_2$ (0.0096 $min^{-1}$). The obtained results showed that the photodegradation efficiencies of the $TiO_2$–$MoS_2$ and C–$TiO_2$–$MoS_2$ samples are significantly higher than those of bare $TiO_2$

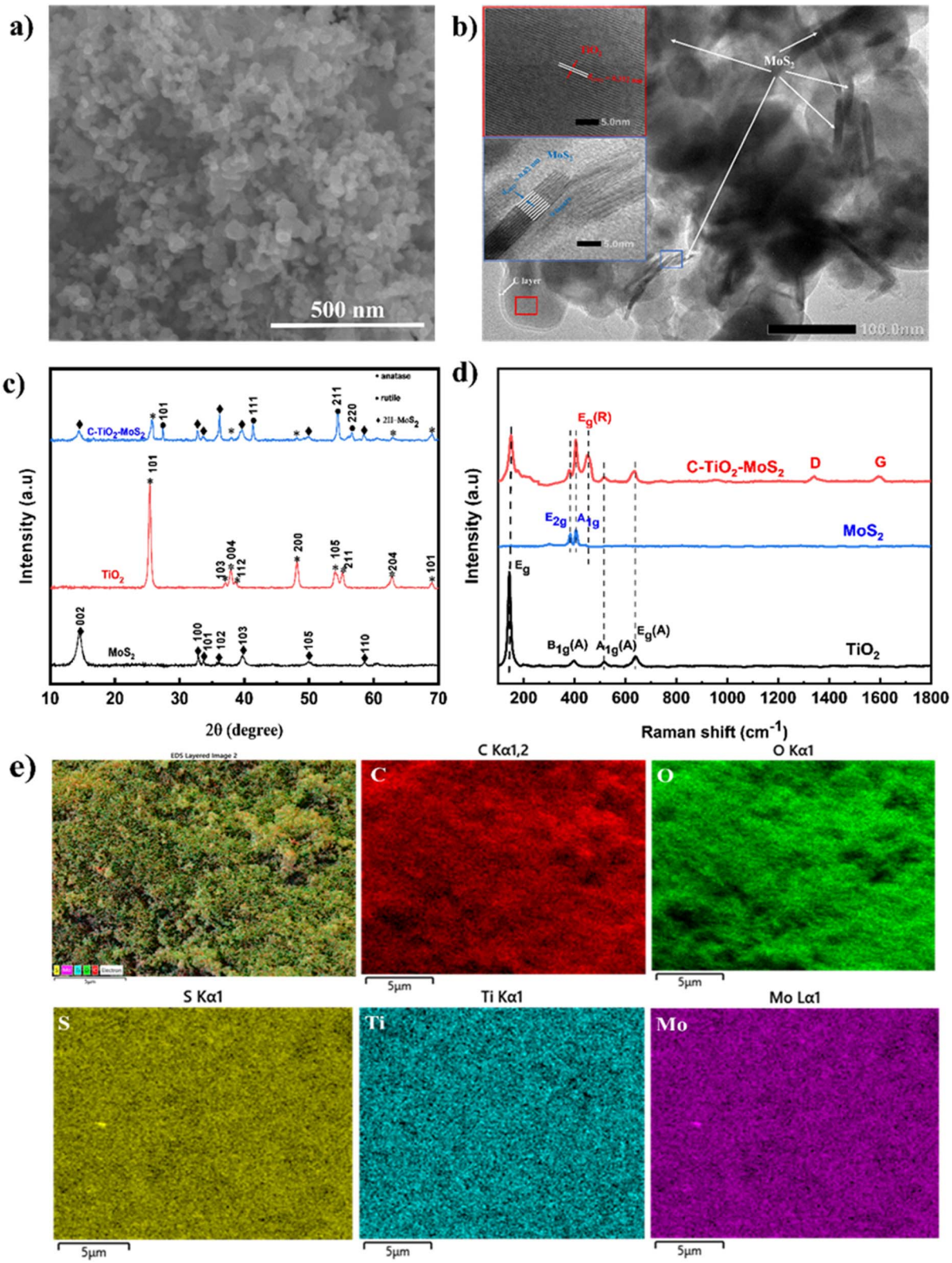


Fig. 2 (a) SEM, (b) HRTEM image, (c) XRD pattern, (d) Raman spectra, and (e) EDS elemental mapping of C–$TiO_2$–$MoS_2$ nanocomposite.

and bare $MoS_2$, C–$TiO_2$. It was evident that the combination of $TiO_2$–$MoS_2$ can provide more active sites and enhance the separation of photogenerated charge carriers due to the formation of type II band alignment between $MoS_2$ and $TiO_2$. Moreover, the introduction of the outer carbon layer created an effective medium for the transport of charge carriers, thereby

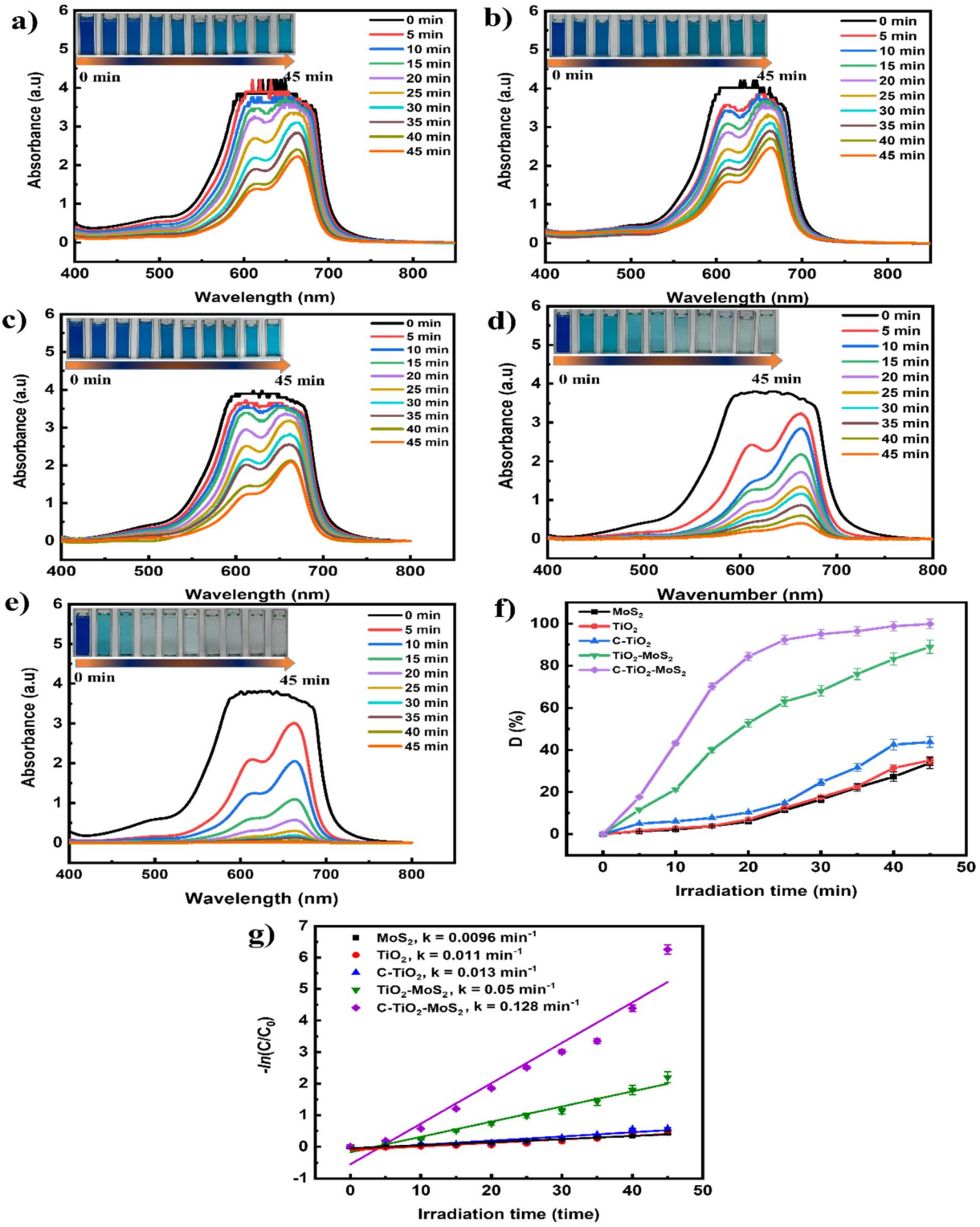


Fig. 3 Time-dependent UV-vis absorption spectra of MB ($10^{-4}$ M) degradation in the presence of (a) bare $TiO_2$, (b) bare $MoS_2$, (c) C–$TiO_2$, (d) $TiO_2$–$MoS_2$ and (e) C–$TiO_2$–$MoS_2$ under UV irradiation. (f) and (g) are MB degradation percentage and degradation rate of the samples, respectively.

improving the photocatalytic activity of C–$TiO_2$–$MoS_2$ nanocomposite. More discussion will be presented in the mechanism section.

The stability of the C–$TiO_2$–$MoS_2$ nanocomposite as a photocatalyst under UV irradiation was also thoroughly assessed over five cycles as seen in Fig. 4. The C–$TiO_2$–$MoS_2$ catalyst

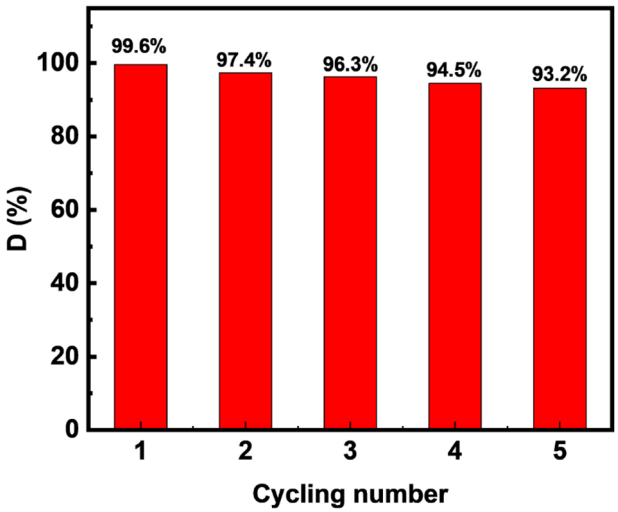


Fig. 4 Five consecutive cycles for the MB photodegradation using C–$TiO_2$–$MoS_2$ nanocomposite.

showed degradation percentages of approximately 99.6%, 97.4%, 96.3%, 94.5%, and 93.2% for MB molecules over the 1st to 5th cycles, respectively. After five cycles, the value of 93.2% was retained, indicating the good stability of C–$TiO_2$–$MoS_2$ nanocomposite.

The photocatalytic performance of the nanocomposite was also systematically evaluated by varying the catalyst dosage, initial pH. When the amount of catalyst was increased from 10 mg to 20 mg/50 mL of MB solution, the degradation efficiency improved as shown in Fig. 5. This is due to the increased number of active sites. However, increasing the nanocomposite loading to 30 mg resulted in a plateau in photocatalytic efficiency, which is attributed to excessive turbidity that hindered light penetration and limited the activation of deeper catalyst layers.

Fig. 6 shows that the initial pH of the solution notably influenced the photocatalytic efficiency, which is attributed to favorable electrostatic interactions between the photocatalyst surface and pollutant molecules. Under acidic condition (pH = 5), the photocatalytic efficiency was decreased while that increased at basic condition (pH = 11), due to catalyst surface charge repulsion or inhibition of reactive species generation.

For real applications, the C–$MoS_2$–$TiO_2$ nanocomposite was also expected to achieve a high degradation efficiency under visible light. As shown in Fig. 7, the MB solution was mostly degraded after 50 min, achieving a degradation efficiency of 99.4% with a corresponding rate constant of $k = 0.091\ min^{-1}$. These values are relatively close to those of the nanocomposite under UV irradiation. This implies that the nanocomposite can operate with high efficiency under both UV and visible light. We made a summary of the photodegradation efficiency of our samples and those of previously reported $TiO_2$-based composites and $MoS_2$-based composites, as shown in Table 1. It should be noted that direct quantitative comparisons are challenging,

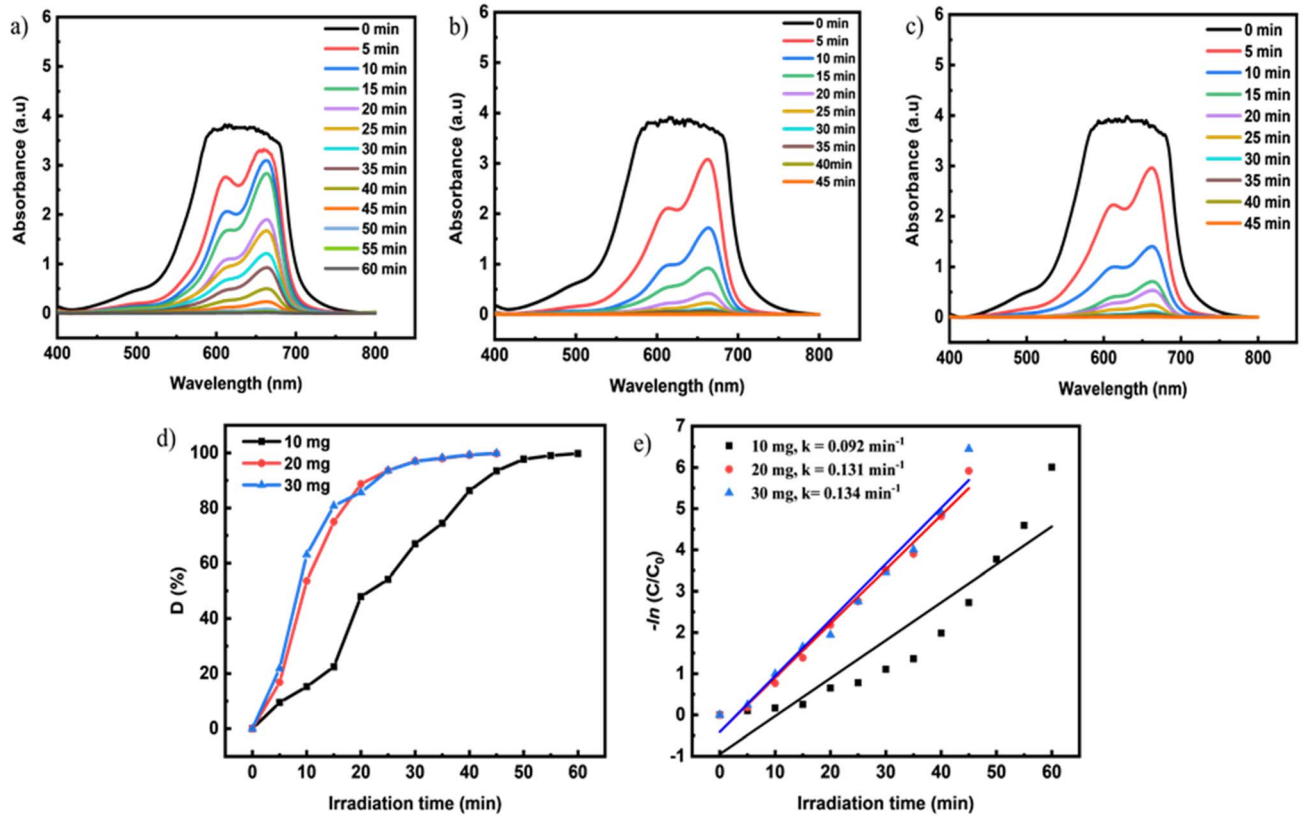


Fig. 5 Time-dependent UV-vis absorbance spectra of MB degradation with varying the amount of the nanocomposite (10, 20, and 30 mg) (a–c). Photodegradation efficiency and constant are presented in (d) and (e), respectively.

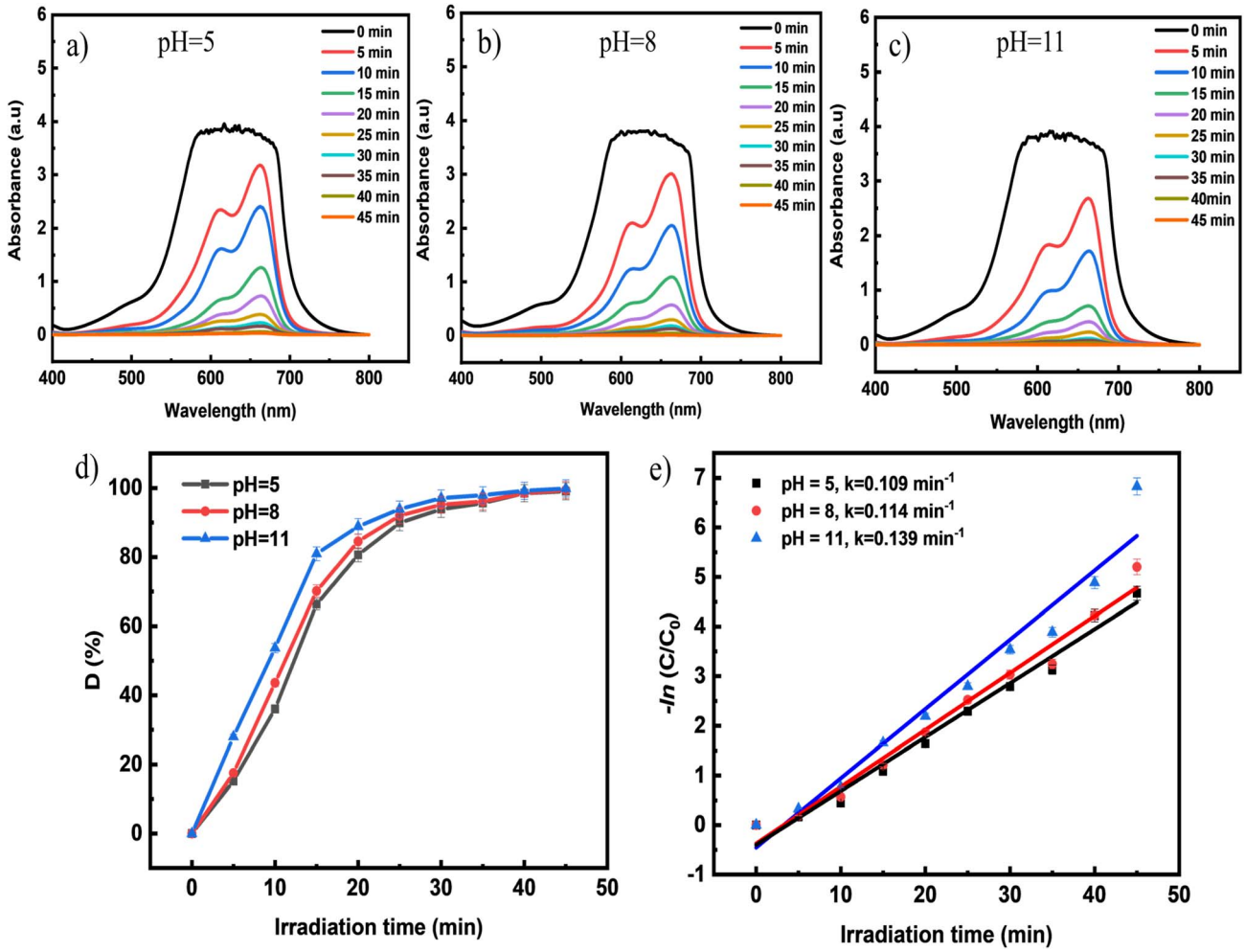


Fig. 6 The effect of initial pH value on photodegradation efficiency. (a–c) Time-dependent UV-vis absorbance spectra of MB degradation with varying the pH of MB solution (5, 8, and 11), respectively. (d and e) Are photodegradation efficiency and constant are presented, respectively.

as experimental conditions such as dye concentration and light source intensity vary considerably among different studies. In this study, thus, we emphasize the ability of the synthesized photocatalyst to effectively degrade methylene blue at significantly higher concentrations ($10^{-4}$ M) than those typically reported (often $\sim 10^{-5}$ M). This demonstrates the robustness and high catalytic capacity of the material under more practical and challenging conditions. While a full comparative study under identical experimental settings would provide further validation, the current findings highlight the uniqueness of our system in handling high dye concentration, which is relevant for real wastewater treatment applications.

To check photocatalytic activity of the nanocomposite with another pollutant, the C–$TiO_2$–$MoS_2$ nanocomposite was further applied to the decomposition of RhB under the same conditions. The same trends were recorded and shown in Fig. S6.†

We try to explain the mechanism behind the enhanced degradation efficiency of the pollutant dyes using our sample under both UV and visible light, we propose the following explanation, illustrated in Fig. 8a. Under UV irradiation, where the photon energy exceeds the bandgap energies of both $MoS_2$ and $TiO_2$, electron–hole pairs are generated in both semiconductors. A significant fraction of the photogenerated electrons from the conduction bands (CB) of $MoS_2$ and $TiO_2$ are rapidly transferred to the carbon layer, which acts as a conductive pathway. This facilitates electron migration and enhances their interaction with surface-adsorbed oxygen molecules. Simultaneously, some electrons from the CB of $MoS_2$ transfer to the CB of $TiO_2$ due to the formation of type-II band alignment. This transfer minimizes electron–hole recombination. The photoinduced holes interact with water molecules or hydroxyl ions on the catalyst surface, leading to the generation of hydroxyl radicals ($^{\bullet}OH$), while the photogenerated electrons reduce molecular oxygen ($O_2$) to form superoxide radicals ($^{\bullet}O_2^-$). Consequently, both $^{\bullet}OH$ and $^{\bullet}O_2^-$ radicals decompose pollutant dyes into carbon dioxide ($CO_2$) and $H_2O$ and intermediates. Under visible light irradiation, electron–hole pairs are primarily generated in the $MoS_2$, while minor electrons are produced in the $TiO_2$ due to the carbon impurity level.[41] This explains why the photodegradation efficiency of the nanocomposite catalyst under visible light is slightly lower than that

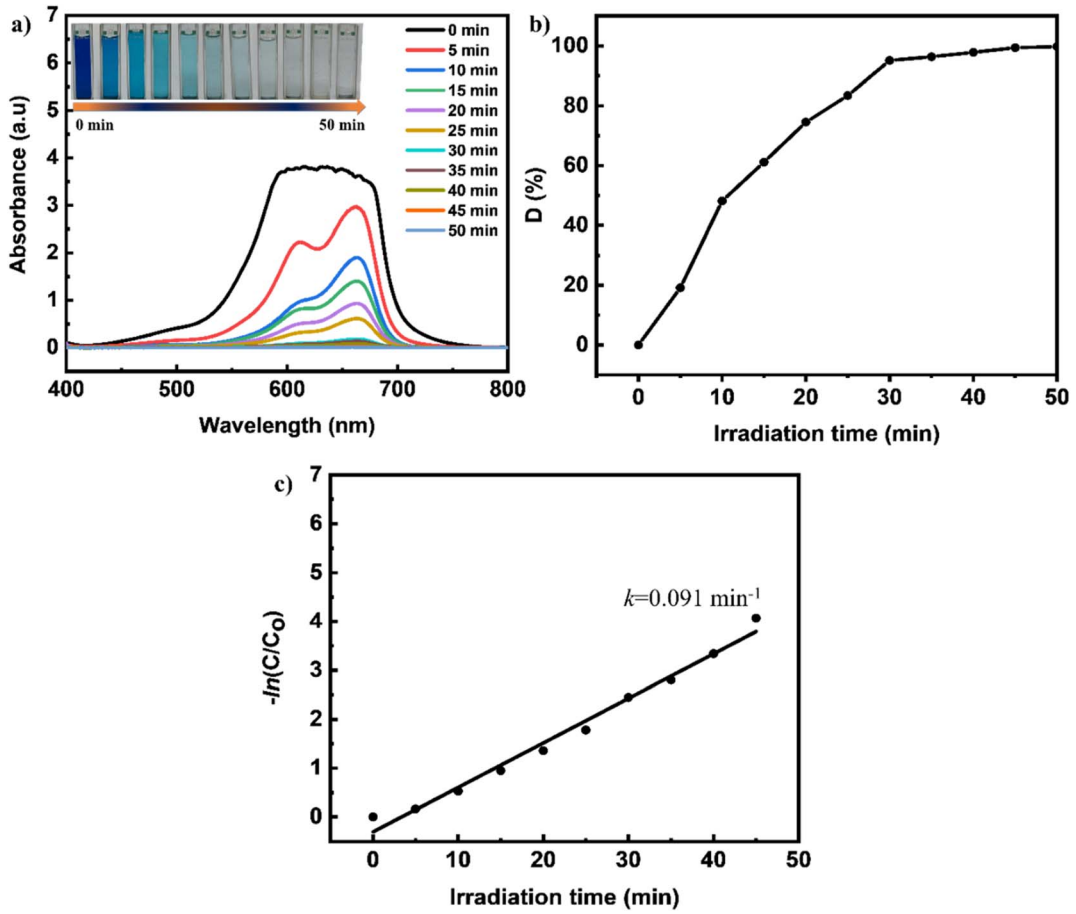


Fig. 7 (a) Time-dependent UV-vis absorption spectra of $10^{-4}$ M MB degradation in the presence of C–$TiO_2$–$MoS_2$ under visible light, (b) MB degradation percentage and (c) degradation rate, respectively.

Table 1 Comparison table of photocatalytic activities of catalysts based on $MoS_2$ and $TiO_2$

| Photocatalyst | Dyes | Concentration (mg $L^{-1}$) | Catalyst loading (g $L^{-1}$) | Light source | Time (min) | Degradation efficiency (%) | Ref. |
|---|---|---|---|---|---|---|---|
| $MoS_2$ | MB | 20 | 0.15 | 200 W Xe lamp [$\lambda > 420$ nm] | 120 | 5.9 | 36 |
| $TiO_2$ | RhB | 5 | 2 | 500 W Xe lamp [$\lambda > 420$ nm] | 180 | 19 | 37 |
| C–$TiO_2$ | MB | 5 | 0.1 | Philips household CFL, 85W, visible light | 120 | 94 | 21 |
| $MoS_2$/$TiO_2$ | MB | 10 | 1 | 500 W, Xenon lamp | 90 | 93.8 | 30 |
| $MoS_2$/$TiO_2$ (P25) | MB | 8 | 0.35 | 300 W, Tungsten lamp, ($\lambda$ = 400–660 nm) | 240 | 32 | 29 |
| $MoS_2$/$TiO_2$ | RhB | 10 | — | 230 W UV lamp, [$\lambda$ = 365 nm] | 150 | 85.3 | 38 |
| $MoS_2$/$TiO_2$ | MB | 20 | 0.33 | UV lamp ($\lambda$ = 360 nm) | 65 | 100 | 39 |
| $MoS_2$/graphene/$TiO_2$ (P25) | RhB | 10 | 0.5 | 150 W solar simulator | 80 | 80 | 40 |
| C–$MoS_2$/$TiO_2$ | MB | 100 | 0.2 | 150 W Xe lamp [$\lambda$ = 300–1900 nm] | 60 | 99 | 31 |
| $MoS_2$ | MB | 100 | 0.2 | 3 W, UV lamp ($\lambda$ = 365 nm) | 120 | 94.7 | This work |
| $TiO_2$ | MB | 100 | 0.2 | 3 W, UV lamp ($\lambda$ = 365 nm) | 120 | 92.8 | |
| C–$TiO_2$–$MoS_2$ | MB | 100 | 0.2 | 3 W, UV lamp ($\lambda$ = 365 nm) | 45 | 99.6 | |
| | | | | 3 W, Xenon lamp ($\lambda$ = 450 nm) | 50 | 99.4 | |
| | RhB | 100 | 0.2 | 3 W, UV lamp ($\lambda$ = 365 nm) | 45 | 99.5 | |
| | | | | 3 W, Xenon lamp ($\lambda$ = 450 nm) | 50 | 99.1 | |

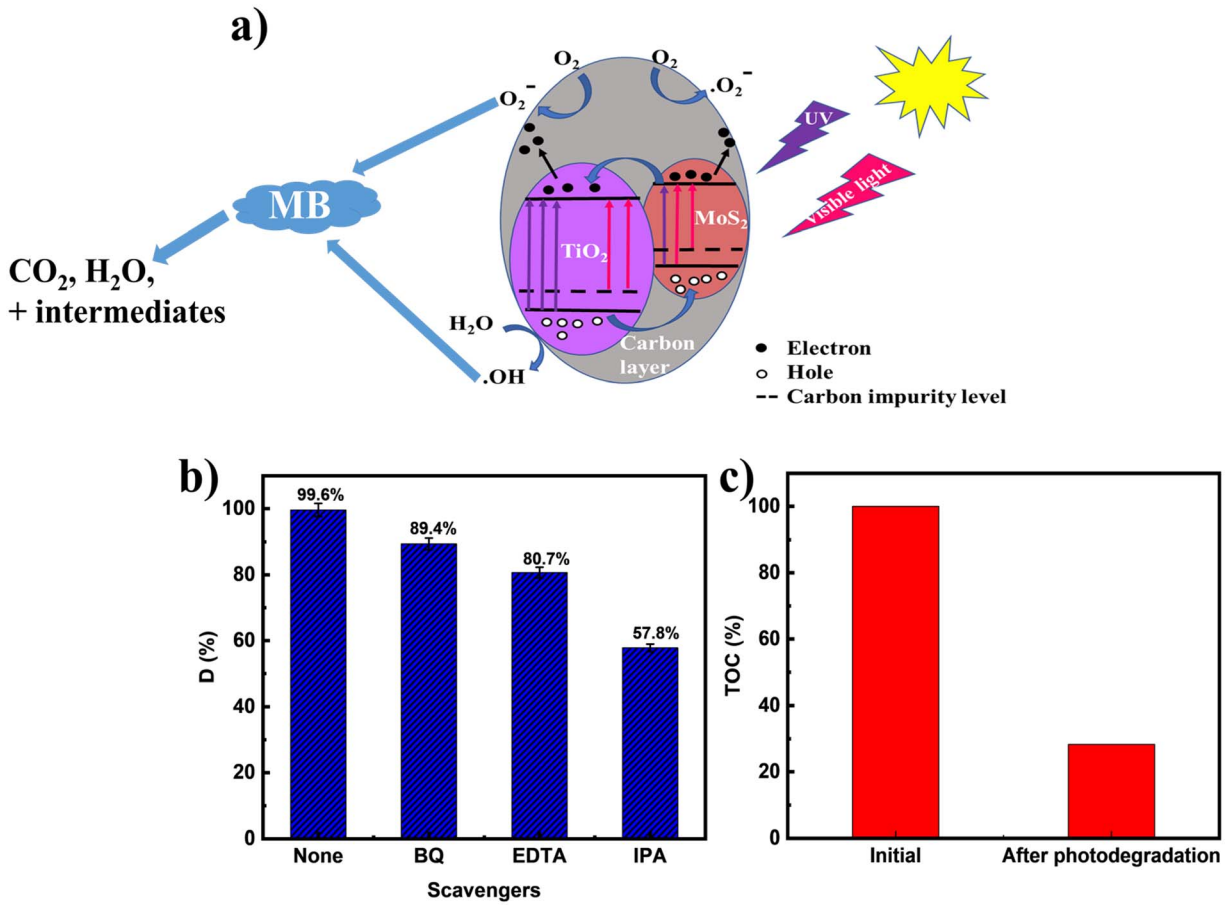


Fig. 8 (a) A proposed mechanism for the degradation of the pollutant dyes by the prepared nanocomposites under light irradiation, (b) reactive species trapping tests, (c) removal of TOC (%) before and after photodegradation.

under UV light. To assess the key roles of the active species involved in the photocatalytic reaction, three distinct scavengers—namely isopropyl alcohol (IPA), ethylenediaminetetraacetic acid disodium salt (EDTA-2Na), and benzoquinone (BQ)—were introduced into the reaction system. These agents were employed to selectively quench hydroxyl radicals ($^{\bullet}OH$), photogenerated holes ($h^+$), and superoxide radicals ($^{\bullet}O_2^-$), respectively.[42,43] As illustrated in Fig. 8b, the degradation efficiency of methylene blue (MB) under UV irradiation decreased from 99.6% to 89.4%, 80.7%, and 57.8% in the presence of BQ, EDTA-2Na, and IPA, respectively. This result indicates that hydroxyl radicals ($^{\bullet}OH$) are the dominant reactive species responsible for MB degradation, whereas holes ($h^+$) and superoxide radicals ($^{\bullet}O_2^-$) contribute to a lesser extent. In addition, the total organic carbon (TOC) analysis was also conducted to evaluate the extent of methylene blue (MB) degradation and its conversion into inorganic end-products. As shown in Fig. 8c, the TOC measurements were used to assess the degree of MB mineralization. The C–$TiO_2$–$MoS_2$ nanocomposite achieved a TOC removal efficiency of approximately 72.7%, indicating that a substantial portion of the MB dye was mineralized into $CO_2$ and $H_2O$ under UV irradiation. These results demonstrate the strong mineralization capability of the C–$TiO_2$–$MoS_2$ photocatalyst.

## 4. Conclusions

In summary, the C–$TiO_2$–$MoS_2$ nanocomposite, incorporating 2D $MoS_2$ exfoliated from bulk $MoS_2$, was successfully synthesized by mixing $TiO_2$–$MoS_2$ nanopowder with the SDC surfactant, followed by thermal annealing at 600 °C in Ar gas. The photocatalytic performance of the nanocomposite was evaluated through the degradation of MB under both UV and visible light irradiation. The results demonstrated excellent degradation efficiency, achieving 99.6% degradation of MB under UV light within 45 minutes and 99.4% under visible light within 50 minutes. The nanocomposite exhibited similar photocatalytic performance when applied to the degradation of high-concentration RhB. These findings highlight a promising strategy for the development of high-performance materials for practical photocatalytic applications.

## Data availability

The datasets used and/or analyzed during the current study are available from the corresponding author upon reasonable request. In addition, all the data generated or analyzed during this study are included in this article.

## Author contributions

Thi Huyen Nguyen: conceptualization, methodology, investigation, formal analysis. Tien Dung Cao: formal analysis, investigation. Thi Phuong Mai: formal analysis, investigation. Van Hau Tran: formal analysis, investigation. Van Trinh Pham: formal analysis, investigation. Van Chuc Nguyen: formal analysis, investigation, project administration. Van Nhat Pham: formal analysis, investigation. Van Tiep Phung: formal analysis, investigation. Ngoc Minh Phan: formal analysis, investigation. Van Tan Tran: investigation. Van Hao Nguyen: formal analysis, investigation. Van Tu Nguyen: supervision, conceptualization, methodology, formal analysis, writing – original draft preparation, validation, writing – reviewing and editing. All authors discussed and approved the paper.

## Conflicts of interest

There are no conflicts to declare.

## Acknowledgements

This work was financially supported by the Vietnam Academy of Science and Technology (VAST) under Project NCXS02.03/24-25.

## References

1 Y. Q. Yang, Z. H. Zheng, D. F Zhang and X. D. Zhang, *Environ. Sci.:Water Res. Technol.*, 2020, **6**, 2454–2464.
2 W. T. Xu, J. N. Chen, Y. Qiu, W. Peng, N. Shi and J. C. Zhou, *Separ. Purif. Technol.*, 2019, **213**, 426–436.
3 T. H. Nguyen, A. S. S. Tran, T. T. Cao, V. Tu Nguyen, V. T. Pham, V. T. Tran, T. Q. X. Le, H. T. Bui, V. H. Tran, T. Do, D. L. Pham, N. M. Phan, H. Abe and V. C. Nguyen, *RSC Adv.*, 2025, **15**(14), 10754–10762.
4 H. Kumari, S. Suman, R. Ranga, S. Chahal, S. Devi, S. Sharma, S. Kumar, P. Kumar, S. Kumar, A. Kumar and R. Parmar, *Water Air Soil Pollut.*, 2023, **234**, 349.
5 M. Mehta, A. P. Singh, S. Kumar, S. Krishnamurthy, B. Wickman and S. Basu, *Vacuum*, 2018, **155**, 675–681.
6 K. Li, Y. Zhong, S. Luo and W. Deng, *Appl. Catal. B Environ.*, 2020, **278**, 119313.
7 F. Bi, Y. Zhang, Z. Zhou, L. Guo, Z. Zhu, B. Liu and X. Zhang, *Molecules*, 2025, **30**(3), 697.
8 Q. Chen, A. Ozkan, B. Chattopadhyay, K. Baert, C. Poleunis, A. Tromont, R. Snyders, A. Delcorte, H. Terryn and M.-P. Delplancke-Ogletree, *Langmuir*, 2019, **35**, 7161–7168.
9 S. Liu, and J. Yu, in *Nanostructured Photocatalysts*, ed. H. Yamashita, H. Li, Springer, Cham, Switzerland, 2016, ch. 10, pp. 187–200.
10 H. Lee, I.-S. Park, H.-J. Bang, Y.-K. Park, H. Kim, H.-H. Ha, B.-J. Kim and S.-C. Jung, *Appl. Surf. Sci.*, 2019, **471**, 893–899.
11 S. A. Ansari, M. M. Khan, M. O. Ansari and M. H. Cho, *Sol. Energy Mater. Sol. Cells*, 2015, **141**, 162–170.
12 A. Zielińska-Jurek, E. Kowalska, J. W. Sobczak, W. Lisowski, B. Ohtani and A. Zaleska, *Appl. Catal. B Environ.*, 2011, **101**, 504–514.
13 S. Sakthivel, M. Shankar, M. Palanichamy, B. Arabindoo, D. Bahnemann and V. Murugesan, *Water Res.*, 2004, **38**, 3001–3008.
14 P. Akhter, F. Ali, A. Ali and M. Hussain, *Diamond Relat. Mater.*, 2024, **141**, 110702.
15 N.-B. Trinh, T. A. Nguyen, S. Van Vu, H.-G. T. Vo, T. N. H. Lo, I. Park and K. Q. Vo, *RSC Adv.*, 2024, **14**, 34037–34050.
16 J. Huang, X. Feng, F. Bi, G. Huang, R. Rao, R. Qiao and X. Zhang, *Sep. Purif. Technol.*, 2025, **359**, 130804.
17 J. Huang, J. Wei, F. Tian, F. Bi, R. Rao, Y. Wang, H. Tao, N. Liu and X. Zhang, *Mater. Today Chem.*, 2024, **41**, 102292.
18 Y. Zhang, Z. Zhou, T. Chen, H. Wang and W. Lu, *J. Environ. Sci.*, 2014, **26**, 2114–2122.
19 A. Purabgola, N. Mayilswamy and B. Kandasubramanian, *Environ. Sci. Pollut. Res.*, 2022, **29**, 32305–32325.
20 Á. Tolosana-Moranchel, A. Manassero, M. L. Satuf, O. M. Alfano, J. A. Casas and A. Bahamonde, *Appl. Catal. B Environ.*, 2019, **246**, 1–11.
21 S. Shen, K. Chen, H. Wang and J. Fu, *Diamond Relat. Mater.*, 2022, **124**, 108896.
22 R. M. Sendão, M. Algarra, E. Ribeiro, M. Pereira, A. Gil, N. Vale, J. C. Esteves da Silva and L. Pinto da Silva, *Adv. Sustainable Syst.*, 2024, **8**, 2300317.
23 W. Ren, Z. Ai, F. Jia, L. Zhang, X. Fan and Z. Zou, *Appl. Catal. B Environ.*, 2007, **69**, 138–144.
24 H. Park, H.-I. Kim, G.-H. Moon and W. Choi, *Energy Environ. Sci.*, 2016, **9**, 411–433.
25 E. Bu, X. Chen, C. López-Cartes, F. Cazana, A. Monzón, J. Martínez-López and J. J. Delgado, *Catal. Today*, 2023, **422**, 114220.
26 H. Dong, D. Chen, K. Wang and R. Zhang, *Nanoscale Res. Lett.*, 2016, **11**, 1–14.
27 K. F. Mak, C. Lee, J. Hone, J. Shan and T. F. Heinz, *Phys. Rev. Lett.*, 2010, **105**, 136805.
28 D. Wang, Y. Xu, F. Sun, Q. Zhang, P. Wang and X. Wang, *Appl. Surf. Sci.*, 2016, **377**, 221–227.
29 G. Chandrabose, A. Dey, S. S. Gaur, S. Pitchaimuthu, H. Jagadeesan, N. S. J. Braithwaite, V. Selvaraj, V. Kumar and S. Krishnamurthy, *Chemosphere*, 2021, **279**, 130467.
30 Z. Tang, L. Xu, K. Shu, J. Yang and H. Tang, *Colloids Surf. A Physicochem. Eng. Asp.*, 2022, **642**, 128686.
31 A. H. Mady, M. A. Mahadadalkar, M. L. Baynosa, D. R. Kumar, A. M. Rabie, J. Lee, W. K. Kim and J.-J. Shim, *J. Colloid Interface Sci.*, 2022, **606**, 337–352.
32 M. M. Ali and K. N. Y. Sandhya, *New J. Chem.*, 2016, **40**, 8123–8130.
33 G. Cao and N. Yi, *ChemistrySelect*, 2020, **5**, 11530–11533.
34 R. Yuan, Y. Guo, I. Gurgan, N. Siddique, Y.-S. Li, S. Jang, G. A. Noh and S. H. Kim, *Carbon*, 2025, **238**, 120214.
35 X. Han, Z. Zhang, Y. Dong, J. Zhao, G. Sun, J. Hu, Q. Xu, X. Zhang, L. Li, T. Toyao, K. Shimizu and N. Zhang, *Chem. Eng. J.*, 2025, **510**, 161609.
36 X. Ni, C. Chen, Q. Wang and Z. Li, *Chem. Phys.*, 2019, **525**, 110398.
37 L. Zhang, Y. He, Y. Wu and T. Wu, *Mater. Sci. Eng. B*, 2011, **176**, 1497–1504.

38 L. Zheng, S. Han, H. Liu, P. Yu and X. Fang, *Small*, 2016, **12**, 1527–1536.
39 I. Tacchini, E. Terrado, A. Anson and M. T. Martínez, *Micro Nano Lett.*, 2011, **6**, 932–936.
40 W. Gao, M. Wang, C. Ran and L. Li, *Chem. Commun.*, 2015, **51**, 1709–1712.
41 Y. Zhang, M. Gong, Xi. Liu, L. Ji, Z. Yang and X. Zhu, *J. Mater. Sci.*, 2019, **54**, 2975–2989.
42 Y. Zhu, J. Xue, T. Xu, G. He and H. Chen, *J. Mater. Sci. Mater. Electron.*, 2017, **28**, 8519.
43 A. Mancuso, S. Mottola, O. Sacco, V. Vaiano and I. De Marco, *Nanomaterials*, 2023, **13**, 3130.